Journal of Materials Chemistry A

ROYAL SOCIETY OF CHEMISTRY

PAPER

View Article Online
View Journal | View Issue

Cite this: J. Mater. Chem. A, 2021, 9, 5588

Electrokinetic effect and H_2O_2 boosting in synthetic graphene/α-FeOOH aerogel films for the generation of electricity†

Wei Wang,[ab] Wenbin Gong,[a] Yaqiong Wang,[c] Guangyong Li,[a] Weibang Lu,[a] Yezi You[d] and Xuetong Zhang*[ae]

Harvesting and transforming water energy into electricity *via* nanostructured materials, which is termed hydrovoltaic power generation (HPG), has attracted increasing interest in the past few decades. However, the current limitation of HPG devices taking advantage of the electrokinetic effect is their poor power density within microwatts per square meter. Herein, a novel catalytic graphene aerogel film decorated with an interlayer catalyst of α-FeOOH was developed successfully. Upon the addition of H_2O_2 to a saline (NaCl) droplet, an exceptionally high voltage of 0.63 V was achieved, which is around 20 times higher than the previously reported value using single-layer graphene. The experimental and theoretical results showed that the high hydrovoltaic performance originates from three contributions. Firstly, the large droplet/graphene interfaces, benefitting from the high specific surface area of the aerogel and the bubbling effect produced by the catalytic decomposition of H_2O_2 *via* α-FeOOH. Secondly, the enhanced electrokinetic effect, *i.e.*, increased hydrated ion radius of NaCl and suppressed shielding effect between cations and anions in the presence of H_2O_2, which dramatically extends the NaCl concentration window from 0.6 M to 5.0 M. Thirdly, utilizing the advantage of electrochemical reactions related to H_2O_2 in the saline (NaCl) droplet to greatly increase the short-circuit current of the HPG device. The outcome of these contributions is a much higher ion utilization efficiency under a high saline concentration, which breaks the output bottleneck of power density caused by using a low saline concentration. Our work extends the device component from single-layer graphene to a 3D porous graphene aerogel, making a significant step forward for the future development of HPG devices.

Received 22nd October 2020
Accepted 19th January 2021

DOI: 10.1039/d0ta10329b

rsc.li/materials-a

Introduction

Graphene aerogel is a three-dimensional porous structure formed through the self-assembly of graphene.[1–3] The excellent chemical and physical properties of graphene combined with the beneficial structure of aerogels provide graphene aerogels with promising applications in the hydrogen evolution reaction (HER),[4–6] high-efficiency thermochemical cells[7] and batteries.[8–11] However, the development of 3D graphene aerogels with desired components, structure and functions for high performance electrochemical energy storage still remains a challenge. Generating electricity using carbon materials through direct contact with water flow has gained extensive interest in the past few years.[12,13] At this early stage, the classical electrokinetic effect theory has been used to explain this phenomenon, where an electric double layer (EDL) will form at the interface when the fluid comes into contact with a solid. The EDL consists of a Stern layer fixed on the solid surface and a diffusion layer rich in counter ions. When the relative movement between the fluid and solid, that is, when the liquid flows on the solid surface or the solid particles move in the liquid, electrophoresis occurs in the form of electrokinetic effects, the movement of particles caused by an electric field, which was discovered in 1807.[14] In 1809, electro-osmosis was reported as an electric field-induced fluid movement[15] and Quincke discovered in 1859 that under external force, the electrolyte passing through the solid surface of a microchannel could generate a voltage along the flow direction, which is called the streaming potential.[16] This represents the first generation of

[a]Suzhou Institute of Nano-tech and Nano-bionics, Chinese Academy of Sciences, Suzhou 215123, P. R. China. E-mail: xtzhang2013@sinano.ac.cn
[b]Nano Science and Technology Institute, University of Science and Technology of China, Suzhou 215123, P. R. China
[c]School of Engineering and Materials Science, Queen Mary University of London, London, E1 4NS, UK
[d]Hefei National Laboratory for Physical Sciences at the Microscale, CAS Key Laboratory of Soft Matter Chemistry, Department of Polymer Science and Engineering, University of Science and Technology of China, Hefei 230026, P. R. China
[e]Division of Surgery & Interventional Science, University College London, London NW3 2PF, UK

† Electronic supplementary information (ESI) available: Simulation procedure, digital photos, stress–strain curves, XRD patterns, more SEM and TEM images, XPS, Raman and FTIR spectra, diagram on possible synthetic mechanism, oxygen productive curves, more open-circuit voltage curves, *etc.* See DOI: 10.1039/d0ta10329b

electricity through the interface interaction between a fluid and solid. The sedimentation potential reported in 1949 explained the directional movement of charged solid or colloidal particles in a liquid.[17] In addition, many studies have reported a flow-induced potential, which is different from the classical electrokinetic effect. For example, in 2003, Sood and Ghosh first experimentally confirmed that electrical signals could be generated by carbon nanotubes when immersed in a flowing liquid.[18] Zhou observed[19] that capillary pressure causes the increasing water in the nano-channels to generate a voltage and directly convert the thermal energy of the surrounding environment into electrical energy based on natural water evaporation, which is different from all the aforementioned electrokinetic effects that require mechanical work. Another way to convert water into electricity is to control its evaporation, resulting in a change in humidity. All the above-mentioned mechanisms together with the numerous substantial studies on various water formats involving fluid, waves, droplets and steam have been summarized as the hydrovoltaic effect.[20]

In recent years, scientists have discovered new patterns of electrokinetic effects. For example, Guo *et al.* found that a potential in the order of millivolts could be generated in the moving direction of a water droplet in monolayer and few-layer graphene based on the potential of electrokinetic effects.[21] Thus far, the reported voltage generated *via* electrokinetic effects is generally in the range of several microvolts to tens of millivolts, which is not adequate for practical applications.[22–26] Given that the interface between a droplet and single-layer graphene is always limited and not all solid–liquid interfaces contribute to power generation, the ion utilization efficiency of droplets is very low in the actual power generation process. Besides, due to the ion screening effect within the Debye length of the electric double layer, the saline concentration of the fluid is generally below about 10^{-3} to 10^{-5} M.[21] The output power density reaches its maximum at a low saline limit, which greatly compromises the practical application of hydrovoltaic devices. Thus, creating more effective droplet/graphene interfaces, enhancing the interaction between the droplet and graphene and breaking the limit of the extra low saline concentration for high performance hydrovoltaic devices remain a challenge in this area.

Herein, we demonstrate a high voltage and power density output using a single saline/H_2O_2 aqueous droplet flowing through a catalytic α-FeOOH/reduced graphene oxide aerogel (CGA) film, producing a voltage of 0.63 V and power density of 47 mW m^{-2}. The voltage is about 20 times higher than that achieved in previous studies.[21] The CGA film with an interlayer growth of fibrous networks was obtained through Fe^{2+} cross-linking and self-reduction. When a pure saline droplet flowed freely through the aerogel film under gravity and capillary force, a potential difference of 0.5 V (with saline (NaCl) concentration of 0.6 M) was generated between two ends of the film. When a small amount of H_2O_2 (40 μL, 15 wt%) was added to the saline solution, the saline/H_2O_2 droplet split into many smaller ones once in contact with the aerogel film owing to efficient catalytic decomposition of H_2O_2 by α-FeOOH. The H_2O_2 contributed to a higher open-circuit voltage due to the massive effective of the droplet/graphene/air three-phase interface by the bubbling effect and the reduced shielding effect between the anions and cations. Besides, the electrochemical reactions related to H_2O_2 in the saline (NaCl) droplet contributed to a greater short-circuit

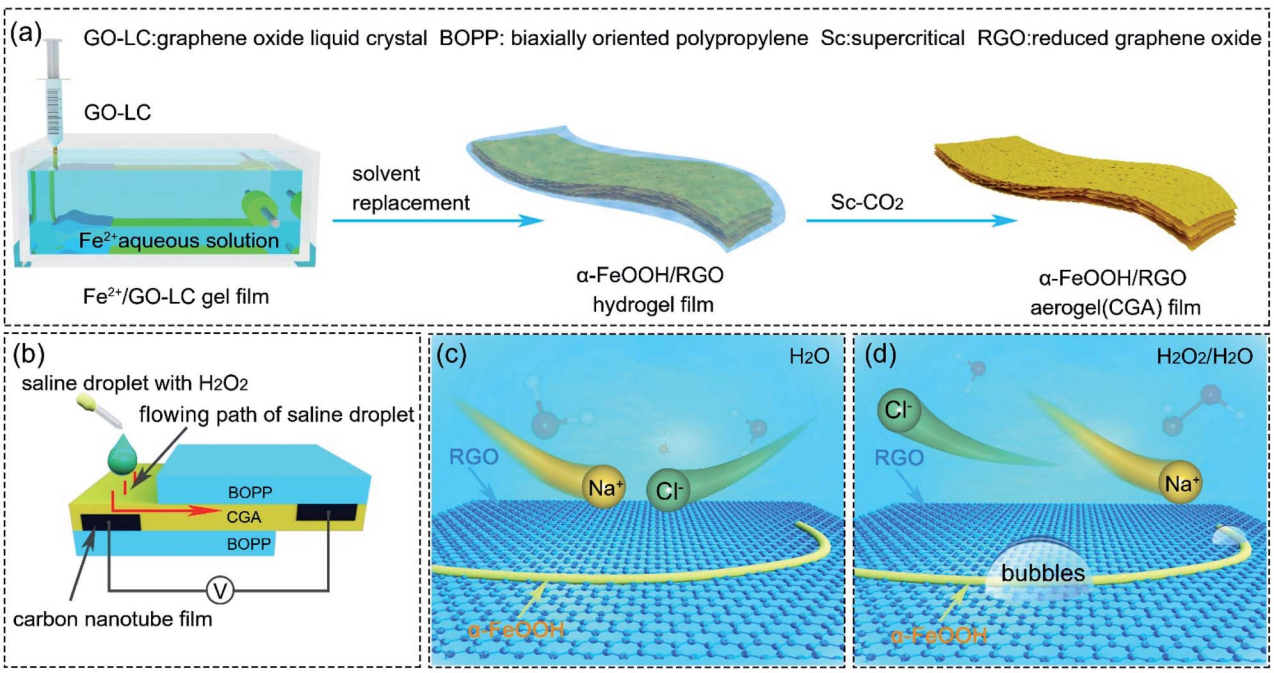

Fig. 1 (a) Schematic description of the fabrication of catalytic graphene aerogel film and (b) its application in a hydrovoltaic power generator (red arrow indicates the flow direction of the saline droplet). (c) NaCl in water and (d) NaCl in H_2O_2/H_2O in the presence of the catalytic graphene aerogel film (α-FeOOH catalyses the decomposition of H_2O to produce oxygen, more details see ESI†).

current in the HPG device. These contributions were demonstrated to enhance the performance of the hydrovoltaic power generation (HPG) device with a maximum output powder density of 47 mW m^{-2} achieved using the high NaCl concentration of 5 M.

Experimental

Synthesis of graphene oxide liquid crystal (GO-LC)

GO was prepared *via* a modified Hummers method using graphite. GO-LC was obtained *via* high-speed centrifugation (11 000 rpm) of GO dispersion for 2 h (Fig. 2a).[7]

Synthesis of catalytic graphene aerogel (CGA) film

The continuous CGA film was assembled *via* the wet spinning method, as shown in the model in Fig. 1a. Briefly, a rectangular spinning channel with a thickness of 500 μm (width of 1.8 mm) was used to inject the GO-LC aqueous dispersion (30 mg mL^{-1}, 9 mL) into the coagulation bath at a spinning rate of 1.5 mL min^{-1}. The coagulation bath was a water solution (500 mL) with 3 wt% $FeSO_4$. After placing it in the coagulation bath for several minutes, the film was transferred together with the bath solution to a box furnace and heated to different temperatures (45 °C, 65 °C and 85 °C) to fully reduce GO to graphene (71–72 wt%) and α-FeOOH (28–29 wt%). The film was washed with absolute ethanol several times followed by supercritical drying with CO_2 (40 °C, 10 MPa) for 12 h. The films were named CGA-4, CGA-6 and CGA-8, which represent CGA synthesized at 45 °C, 65 °C, and 85 °C, respectively.

Manufacturing of hydrovoltaic power generation (HPG) device using CGA film

The as-prepared CGA film was cut to a standard size (1 cm × 1 cm). As shown in Fig. 3a, electrode pads were placed at the upper and lower edges of the film, and biaxially oriented polypropylene (BOPP) was used to encapsulate the electrode (1 cm × 0.2 cm) and the CGA film. The droplet dropping position was reserved on the opposite side of the electrode to ensure that the droplets did not touch the electrode during interaction with the film.

Effects of electrochemical reactions

A large number of saline droplets was added to CGA to completely fill it. At this time, the open-circuit voltage of the HPG device containing CGA was tested. We also immersed the entire HPG device into NaCl (1 M) solution with or without H_2O_2, and applied a constant potential (0.7 V to mimic the

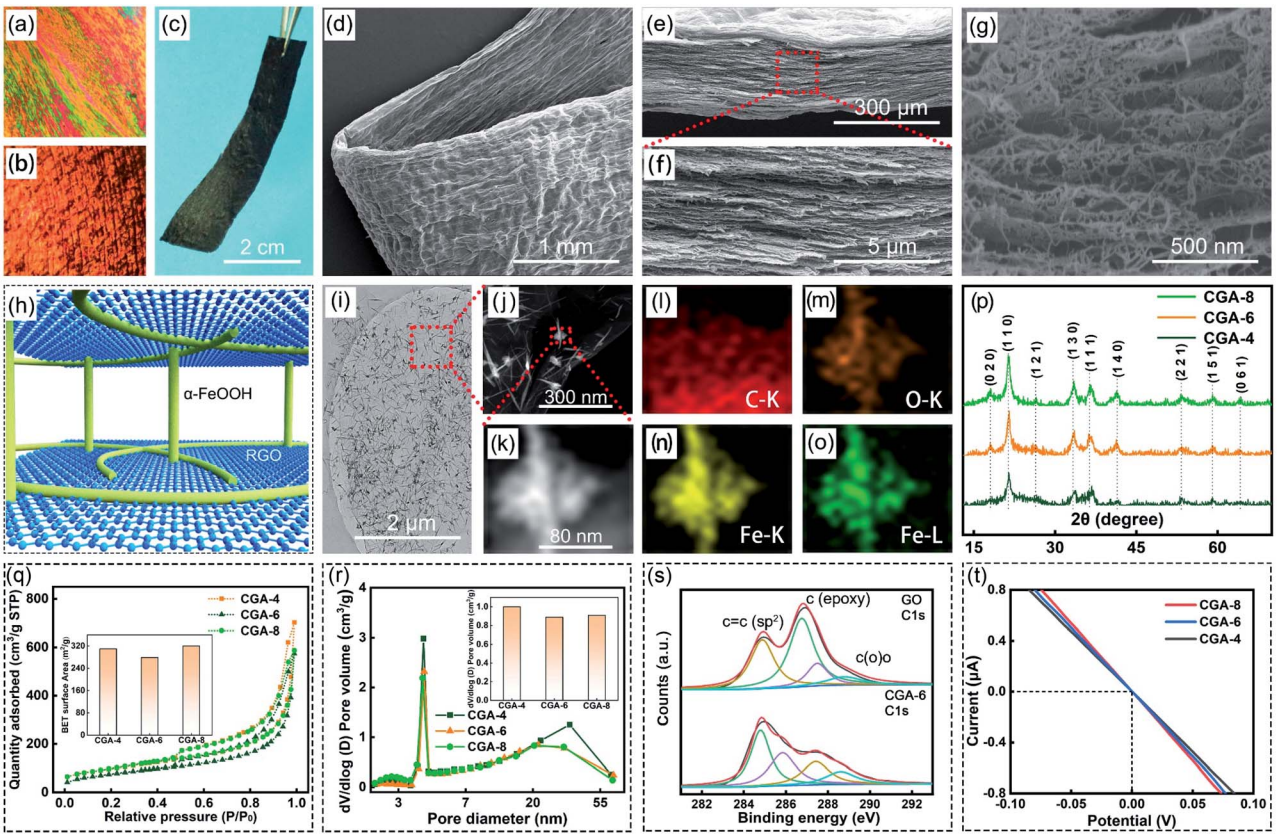

Fig. 2 (a) POM image of GO-LC loaded in a microscope slide, at 30 mg mL^{-1}. (b) POM image of RGO gel film. (c) CGA digital photo image and (d) SEM image of the CGA film in the bent state. (e–g) SEM images of the facture surface of the CGA film at different magnifications. (h) Schematic diagram of the CGA film. (i) TEM image of the CGA film, (j and k) its locally magnified images, and (l–o) respective element mapping images. (p) X-ray diffraction (XRD) patterns of CGA-4, CGA-6, and CGA-8. (q) Nitrogen adsorption–desorption isotherms and (r) pore size distribution curves of CGA-4, CGA-6, and CGA-8. (s) Core-level C 1s XPS spectra of the GO and CGA-6. (t) Linear *I*–*V* curves of CGA-4, CGA-6, and CGA-8.

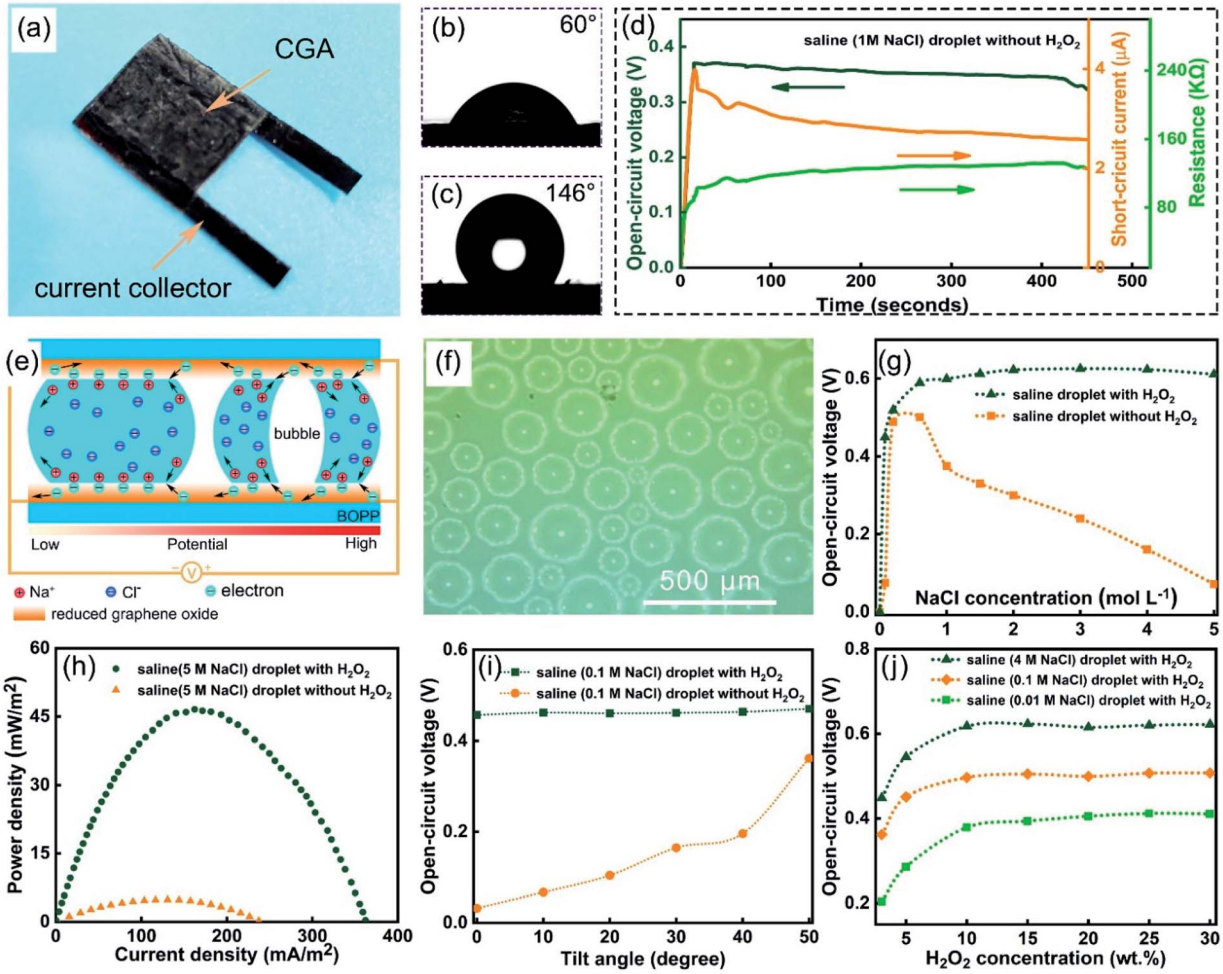

Fig. 3 (a) Digital photo of hydrovoltaic power generation (HPG) device. Contact angle images of CGA (b) and RGO (c). (d) Measured open-circuit voltage, short-circuit current, and resistance profiles from HPG device by dropping a 60 μL of saline (1 M NaCl) droplet. (e) Schematic diagram on the hydrovoltaic power generation in the absence (left) and presence (right) of H_2O_2 in the CGA film. (f) Large number of spherical bubbles were generated when saline droplets containing H_2O_2 touch the surface of CGA film. (g) Open-circuit voltage of HPG device triggered by saline droplets without or with H_2O_2 (15 wt%) at different concentrations of NaCl. (h) Output power density of the HPG device triggered by 5 M saline droplets without or with H_2O_2. (i) Effect of tilt angle on open-circuit voltage triggered by saline droplets without or with H_2O_2. (j) Concentration of H_2O_2 affects the open-circuit voltage at the same concentration of NaCl (0.01 M, 0.1 M and 4 M NaCl).

potential generated *via* the electrokinetic effect) and tested the relationship curve between the current and time.

Effects of liquid–solid interface and three-phase interface

We used saline (1 M NaCl) droplets of different volumes (20 μL, 40 μL, 60 μL, 80 μL, and 100 μL) on the RGO film with an inclination angle of 50° to obtain the same initial sliding speed at the same height (8 cm) and tested the open-circuit voltage at both ends of the RGO film. The relationship between the open-circuit voltage of the saline droplets on the RGO film and the area of the liquid–solid interface or the perimeter of three-phase interface was analyzed to discuss the effects of the liquid–solid interface and gas–solid–liquid interface three-phase interface.

Effects of the flowing speed and number of saline droplets

Saline (1 M NaCl) droplets with the same volume were flowed on the RGO film at different heights to obtain different speeds, and the relationship between the open-circuit voltage at two ends of the RGO film and the flowing speed of the saline droplets was measured. Different numbers of saline (1 M NaCl) droplets of the same volume were flowed on the RGO film at the same height to obtain the same speed, and the relationship between the open-circuit voltage at the two ends of the RGO film and the number of saline droplets was also measured.

Results and discussion

Fig. 1a illustrates the fabrication process of the CGA films *via* a special liquid crystal wet spinning strategy followed by supercritical fluid drying with CO_2. Oriented reduced graphene oxide (RGO) gel films were assembled by colloidal sheets, which were obtained parallel to the wet spinning direction under the shear flow stress of a specially made rectangular channel.[27] The fluid graphene oxide liquid crystal (GO-LC) suspensions changed to gel films rapidly by shear flow-induced orientation

and subsequent coagulation.[27] GO-LC was injected with a given speed into the coagulation bath (3 wt% $FeSO_4$ aqueous solution) from the spinning channel. The polyvalent Fe^{2+} in the coagulation bath solution could strengthen the coordinative crosslinking between two adjacent graphene layers of GO-LC. Fig. 1b illustrates the HPG device setup. The biaxially oriented polypropylene (BOPP) was used to encapsulate the CGA film to ensure that the water droplet flowed through the inside rather than the surface of the CGA film, and a small piece (1 cm × 0.2 cm) of carbon nanotube (CNT) film with (electro-)chemical inertness was used as the current collector.[28] When a saline droplet with H_2O_2 comes into contact with the CGA film, H_2O_2 is quickly catalyzed and decomposed into oxygen bubbles, dividing the droplet to many smaller ones. In the hydrogen peroxide solution, sodium ions and chloride ions can be separated further, which is mainly attributed to the solvation ability of hydrogen peroxide (Fig. 1c and d).

Fig. 2a shows the polarized optical microscopy (POM) image of GO-LC loaded on a microscope slide and Fig. 2b shows the POM image of the RGO gel film. The GO dispersion (30 mg mL^{-1}) showed the typical striated texture and vibrant chromatic colour under POM, revealing its properties of nematic liquid crystals. Observed under POM, the anisotropic oriented RGO gel films exhibited a large-scale fibrous LC texture along the wet spinning direction. The golden yellow texture of the RGO gel films caused by the significantly decreased transmittance of the polarized light in the vertical region was different from the original GO-LC color.[27] Based on the wet-spinning process, the macroscopic assembled CGA film (Fig. 2c) was achieved from the RGO gel film after supercritical drying with CO_2. The as-prepared CGA film possessed a suitable bending strength, as depicted in Fig. 2d. This inspired us to assemble it into devices with an arbitrary shape. The CGA film has a highly ordered layered structure in a cross-section along the plane direction (Fig. 2e and f and S1†). According to Fig. 2g and S2,† it can be seen that short fibers penetrate and connect the RGO sheets through the entire aerogel. As shown in Fig. 2h, after the reduction of GO, a bridge was formed between the adjacent RGO sheets by the short fibers, forming a typical rivet structure. In the fabrication process of the CGA film obtained by the spinning strategy, Fe^{2+} ions slowly diffused into the graphene oxide layers to form a fiber, which crossed and grew much longer along the reduced graphene oxide sheets. Considering that no fibrous α-FeOOH was observed (Fig. S3†) during the synthesis of the composite aerogel directly in a beaker, it can be concluded that the growth of the fibrous α-FeOOH in the original composite aerogel may be related to the diffusion process of the iron source during spinning. The CGA film designed by this rivet structure had a strong fracture strength (2.71 MPa) and Young's modulus (34.74 MPa), as depicted in Fig. S4.† Fibers were also formed on the graphene sheets, as shown in Fig. 2h, which were also confirmed in the transmission electron microscopy (TEM) image (Fig. 2i) and element mapping of the fibers (Fig. 2j–o), revealing the existence of Fe and O. The X-ray diffraction (XRD) pattern (Fig. 2p and S5†) confirmed that the fibers are α-FeOOH (JCPDS no. 29-0713). The α-FeOOH fibers show a typical dislocation-driven mechanism, resulting in a morphology with a darker axis line at the center of the fiber, as can be seen in TEM images in Fig. S6,† which is consistent with that reported in a previous study.[29] The CGA films are a network structure of nanoporous solid materials, with an extremely low density (62–70 mg cm^{-3}) and lightweight characteristics (Fig. S7†). The Brunauer–Emmett–Teller (BET) analysis showed that the 3D interconnected porous structure endows CGA with a high specific surface area, S_{BET}, of 320 $m^2\ g^{-1}$ and pore volume of 1.07 $cm^3\ g^{-1}$, which will provide large droplet/graphene interfaces (Fig. 2q and r) in the HPG device. In the X-ray photoelectron spectroscopy (XPS) characterization of the CGA-6 and GO, as shown in Fig. 2s and S8,† the photoelectron lines at 285 eV, 531 eV, and 711 eV in the wide-scan XPS spectrum confirm the existence of high levels of C, O, and Fe elements in CGA, which belong to C 1s, O 1s, and Fe 2p, respectively. Also, the C 1s peak at 284.5 eV, which is characteristic of C=C bonds, has a higher intensity in CGA, while the C 1s peak at 286.5 eV which is characteristic of epoxy C–C bonds, has a lower intensity in CGA. The C 1s component of carboxylic acid moved from 289.4 eV to 288.8 eV, exhibiting complexation between the metal and the carboxylic acid. With Fe^{2+} crosslinking, the tensile strength properties were also significantly strengthened compared to GO (Fig. S3†). In the Raman spectra (Fig. S9†), the intensity ratio of the well-documented D band and G band of the aerogel increased after reduction compared with that of GO, further indicating the reduction of GO to RGO.[30] When comparing the Fourier transform infrared (FT-IR) spectra of GO and CGA in Fig. S10,† it can be found that the absorption bands of carbonyl at 1740 cm^{-1} and epoxy C–O at 1235 cm^{-1} of GO significantly decreased for CGA, indicating the effective reduction of GO. It is reasonable to speculate that the CGA films were assembled through the reduction of the epoxy C–C functional groups on GO by Fe^{2+} with α-FeOOH formed (Fig. S11†). The electrical properties of the as-prepared CGA films were also investigated, with the obtained I-E curve shown in Fig. 2t. They all show a typical linear feature, demonstrating the conductive nature of the CGA film, which can be used in HPG.

A hydrovoltaic device was constructed using the as-prepared CGA film, as shown in Fig. 3a and S12.† Hydrophilicity is a critical property of a hydrovoltaic device. The formation of hydrophilic α-FeOOH fibers across the RGO layers dramatically improved their hydrophilicity and the obtained CGA film exhibited a low contact angle of 60°, as shown in Fig. 3b. When HI was used instead of Fe^{2+} to reduce the graphene oxide, the obtained RGO showed a very high contact angle of 146° (shown in Fig. 3c), which is not suitable for HPG devices. Fig. 3e depicts the mechanism of the electricity generation from a pure saline droplet (left) and the enhanced electricity production after the addition of H_2O_2 to the saline droplet (right). The hydrovoltaic electricity generation is based on the electrokinetic effect. All the ions in the solid–liquid interface in the middle of the droplet are not adsorbed or desorbed when the droplet is flowing, and thus there is no contribution to the V_{oc}. In fact, it happens between two ends of the droplet/graphene interface, that is, between the two gas–solid–liquid three-phase interface. The two ends are the core regions for adsorbing and desorbing

ions. When a saline droplet flows through the graphene layers, the hydrated Na^+ at the front of the droplet is adsorbed by Coulomb force and can attract the electrons in the graphene. Meanwhile, the terminal ions desorb and release electrons back into the graphene. This process results in a decrease in the electron density at the front of the graphene and droplet interface, resulting in an increase in the graphene potential and an increase in the electron density at the end, which reduces the potential of graphene.[21,31] This potential difference between the two ends of the droplet generates a voltage output. An EDL exists in both the solid–liquid interface and the three-phase interface, but only the ions adsorbed and desorbed at the three-phase interface of the effective interface can contribute to the V_{oc}. Upon the addition of H_2O_2 to the saline droplet, the catalytic decomposition of H_2O_2 produces a lot of gas bubbles (as observed under an optical microscope, shown in Fig. 3f) and separates the big saline droplet to many smaller ones (Fig. S13† and ESI Note 1).[32,33] This provides much more three-phase interface regions, as indicated in the molecular dynamics simulation conducted for big and small water droplets. The results (shown in Fig. 4a) suggest that smaller-sized droplets have an increased proportion of interfacial H_2O molecules to the total droplet molecules (Fig. 4a). The definition of utilization efficiency is the ratio of molecules at the three-phase interface (gas–solid–liquid interface) to the molecules at all the solid–liquid interfaces (including solid–liquid interface and gas–solid–liquid interface). We performed molecular simulation calculations and the results showed that the smaller the droplet, the higher the molecular utilization rate. When the droplet has only 100 molecules, the utilization rate can reach more than 80%. With more molecules in the droplet, the molecular utilization rate will be greatly reduced. This means that with same volume of the solution flowing through the graphene layers, much more effective contact interfaces are formed with the addition of H_2O_2, and thus a higher electricity production efficiency can be achieved. The influence of the liquid–solid interface and three-phase interface was further revealed. We analyzed the linear relationship between the open-circuit voltage of the saline droplets on the RGO film and the area of the liquid–solid interface or the perimeter of the three-phase interface.

The results showed that the open-circuit voltage and the perimeter of the three-phase interface are closer to a linear relationship, that is, the voltage is more dependent on the three-phase interface (Fig. S14†). Fig. 3d and S15† show the measured open-circuit voltage (V_{oc}), short-circuit current (I_{sc}), and resistance of the CGA film device measured when a saline droplet without H_2O_2 flowed through. It can be seen that within 8 min, the V_{oc} of the HPG device remain almost stable, while the I_{sc} exhibited a gradual decrease. This is because the device becomes gradually hydrated with time, which leads to an increased internal resistance and the current decreases correspondingly. The CGA was filled with saline solution, and the liquid no longer flowed. At this time, there was no voltage output at both ends of CGA (Fig. S16a†). Compared with previous experiments, only the flow was different, which means

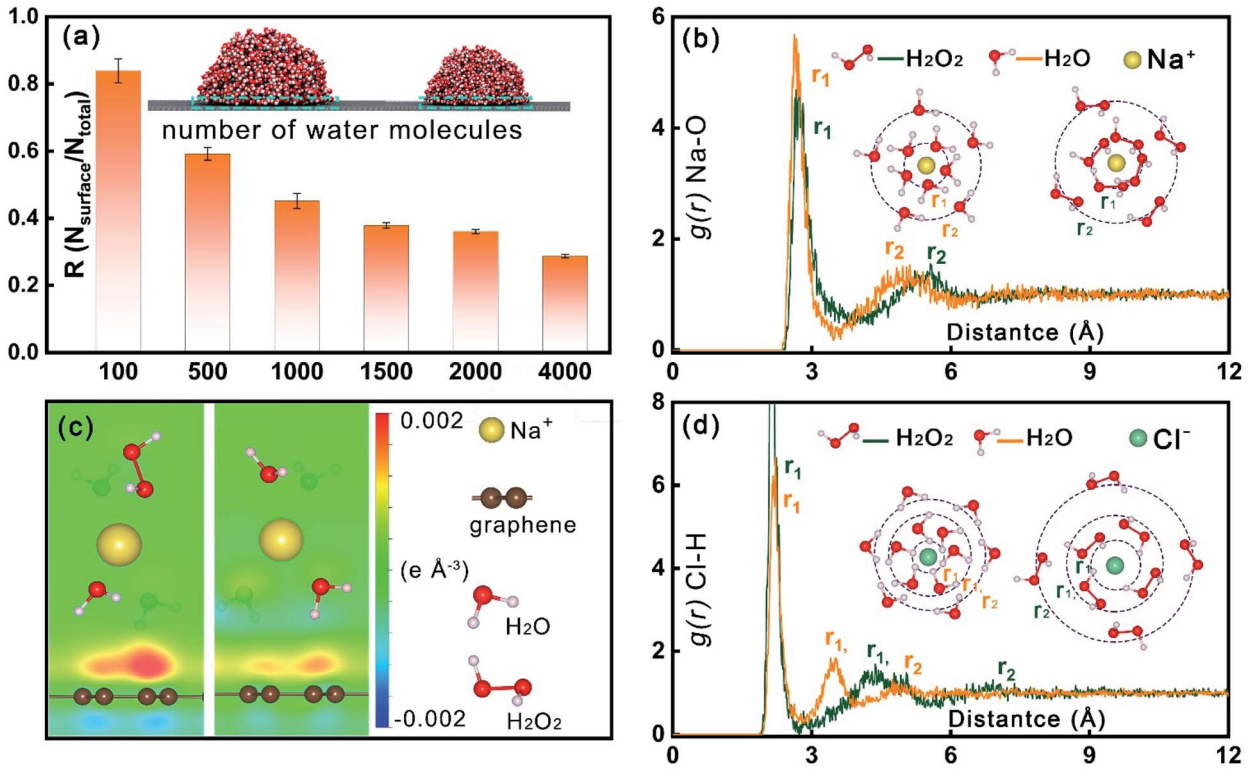

Fig. 4 (a) Count ratio of interfacial H_2O molecules to total molecules varies with the size of water droplets. RDF for Na–O (b) and Cl–H (d) in H_2O or H_2O_2, and (c) charge redistribution of graphene upon adsorption of Na ions in pure H_2O and a mixture of H_2O/H_2O_2.

that electrochemical reactions (such as the reduction of hydrogen peroxide to water, oxidation of hydrogen peroxide to oxygen, oxygen reduction reaction, reduction of α-FeOOH, oxidation of RGO, and galvanic corrosion of the current collector) were not the source of the output voltage. Fig. S16b† shows that the short-circuit current value of the HPG device completely immersed in NaCl solution with H_2O_2 was 35% higher than that of NaCl solution without H_2O_2 under the constant potential of 0.7 V much lower than the voltage of splitting water, the reversible potential (E_{rev}) of the thermodynamic value for the water splitting reaction, $H_2O = H_2 + 1/2O_2$, is $E_{rev} = 1.23$ V (ref. 34), indicating that these possible electrochemical reactions greatly increase the short-circuit current of the HPG device. The open-circuit voltage of the HPG device exists when the circuit is not connected, and the possible electrochemical reactions do not form a loop current at both ends of the HPG device, which will not contribute to the open-circuit voltage at moment. The short-circuit current of the HPG device is generated by the voltage applied to the external circuit and a directional current inside the HPG is generated, and the possible electrochemical reactions can contribute to a larger short-circuit current by the loop current. Briefly, some of these electrochemical reactions do not affect the open-circuit voltage but increase the short-circuit current of the HPG device. Fig. 3g presents the V_{oc} achieved at different NaCl concentrations using pure saline and saline/H_2O_2 solution. When a pure saline droplet was used, the open circuit voltage increased initially, reaches a peak value of 0.5 V at 0.6 M with a calculated power density of 1.6 mW m^{-2} and decreased dramatically with an increase in NaCl concentration. When H_2O_2 was added, the device maintained a high voltage output with an increase in NaCl concentration and reached a peak value of 0.63 V at 3 M. It showed a slight decrease when the NaCl concentration was increased from 3 M to 5 M, indicating that the addition of H_2O_2 can significantly reduce the shielding effect but cannot eliminate it. With the addition of H_2O_2, the power density output was greatly enhanced and reached an exceptionally high value of 47 mW m^{-2} at 5 M, which is nearly 10 times higher compared to the maximum output power density achieved without the use of H_2O_2 (Fig. 3h and ESI Note 2†). The experiments verified the difference between when the saline droplet contains H_2O_2 and when it does not. When H_2O_2 was present, the peak current increased by 50% and the duration increased slightly (Fig. S17†).

The effect of H_2O_2 concentration on the V_{oc} was also studied in the presence of 0.01 M, 0.1 M and 4 M NaCl saline solutions, as shown in Fig. 3j. The results show that in three different concentrated saline solutions, the V_{oc} showed an analogous changing trend with an increase in H_2O_2 concentration. They all exhibited a fast increase initially, and remained stable when the H_2O_2 concentration reached 15 wt%. The effect of the tilt angle of the CGA film device on the electricity generation was also investigated. Fig. 3i shows the V_{oc} produced using pure saline solution and saline H_2O_2 solution (0.1 M NaCl) with different tilt angles. With the addition of H_2O_2, the V_{oc} exhibited a stable output value of ~0.46 V through the whole tilt angle range from 0° to 50°, whereas the output using pure saline solution could only reach a relatively lower value of 0.36 V when the tilt angle increased to 50°. This demonstrates the great enhancement brought by the addition of H_2O_2. The results show that when pure saline is used, gravity is a major factor affecting the voltage, while its effect becomes very small when H_2O_2 is used. The effect of the droplet volume was also studied and results show that with a larger droplet volume, the flow and diffusion time of the droplet became longer and the V_{oc} increased at the same time (Fig. S18†). It was difficult to decouple the contribution of effects of separating the water and forcing the flowing of water in CGA. Thus, additional experiments were designed for droplets flowing on the surface of the RGO film. The flowing speed was obtained by designing the saline (1 M NaCl) droplet to slide down at different heights. The relationship between the different flowing speeds of the saline (1 M NaCl) droplet and the open-circuit voltage was tested (Fig. S19a†). The result showed that the greater the speed, the greater the voltage output. The relationship between the number of droplets and the open-circuit voltage was also tested (Fig. S19b†), and the results showed that the number of droplets was proportional to the voltage. The comparative experiments showed that the separation of large droplets into small droplets and the flowing speed *via* gravity had almost the same effect. However, the extra moving speed of droplet *via* bubbling (much less than 0.01 mm s^{-1}) was much lower than the above-mentioned flowing speed (more than 0.37 m s^{-1}), which indicates that the separation of the droplet in the aerogel exhibits a large contribution to the voltage output. The ambient test temperature of HPG device affected the V_{oc} with a saline droplet (0.1 M NaCl). With an increase in temperature, the V_{oc} increased gradually (Fig. S20†). The V_{oc} of HPG produced by using solutes of different ions was also obtained. The results show that solutions of different ions can generate voltage and have almost the same effect as NaCl. (Fig. S21†). To explore the effect of the surface oxygen functional groups on graphene on the results, CGA was heated at 600 °C for 1 h to remove the surface oxygen functional groups and assembled into a hydrovoltaic power generation (H-HPG) device. As shown in Fig. S22,† the surface oxygen functional groups on graphene did not obviously contribute to the performance considering the comparative experiments.

The electric double layer theory is well accepted to explain the electrokinetic effect. According to this theory, a shielding effect between ions exists when the space between them is within the Debye length, which is inversely proportional to the square root of the ion concentration (Fig. S22†). In a high ion concentration system, the anion has a strong shielding effect on the cation.[21] This shielding effect can hardly be eliminated from aqueous systems but can be weakened through solvent manipulation. The radial distribution function (RDF) was used to study the interactions between ions in the saline and saline/H_2O_2 solution to understand the high ion concentration allowed after the addition of H_2O_2 (ESI Note 3†). Cations and anions exist in the solvent in a hydrated form, which can be clearly seen from sharp peaks in the calculated radial distribution function (RDF) of Na–O (Fig. 4b) and Cl–H (Fig. 4d). The different peaks in RDF are assigned to different layers of H_2O or H_2O_2 molecules. The sizes of the hydrated Na^+ and Cl^- are determined by the second-layer solvent molecules given that the first layer molecules are part of the hydrated ions. The RDF of

Na–O shows that the size of hydrated Na^+ in H_2O_2 is about 0.4 Å larger than that in H_2O, while dramatic size differences of Cl^- exist in H_2O and H_2O_2, where the latter (6.9 Å) is about 2 Å larger than the former (4.9 Å). Therefore, the distance between Na^+ and Cl^- in H_2O_2 is on average of ~2.4 Å larger than that in H_2O, which can greatly reduce the shielding effect, allowing a higher ion concentration to be used for higher voltage output. According to the mathematical relationship[21] between the Debye length of the size of the hydrated ion and ion concentration, the Debye length of the size of the hydrated ion only changes by 30%, while the ion concentration changes be 10 times (Fig. S23†). The charge transfer analysis clearly indicates that the weakened shielding ability of anions makes the hole doping of graphene become heavier under the condition of a high ionic concentration (Fig. 4c). Furthermore, several experiments were carried out to test the repeatable performance of the device, and the results were convincing after 10 consecutive tests (Fig. S24†). Besides, with a reduction in the H_2O_2 content, the device could be used more reliably. We analyzed the HPG device before and after 10 experiments *via* XRD, specific surface area S_{BET} and fracture strength, and the results (Fig. S25†) showed that the device maintained good stability and reusability. As shown in Fig. S26,† four assemblies of HPG in series could light a specific symbol when connected to a liquid crystal display (LCD).

Conclusions

In summary, we obtained a novel catalytic α-FeOOH/reduced graphene oxide aerogel film for application in high performance hydrovoltaic device using a special liquid crystal wet spinning strategy. This is the first report on the use of aerogel materials and electrokinetic effect resulting in the generation of electricity. The graphene aerogel film supplied a porous structure with a massive graphene surface and the α-FeOOH nanofibers worked as catalytic sites for the decomposition of H_2O_2. The addition of H_2O_2 to the saline solution was found to greatly enhance the output voltage from 0.08 V to 0.61 V, with an exceptionally high power density of 47 mW m^{-2} achieved. This was attributed to the bubbling effect resulting from the massive effective droplet/graphene interfaces and the high ion utilization efficiency under a high saline concentration, benefitting from the reduced shielding effect between the anions and cations. Also, the electrochemical reactions related to H_2O_2 in the saline (NaCl) droplet contributed to a greater short-circuit current. Our work proposes a new direction for design and synthesis of aerogel-based high performance hydrovoltaic devices, which are promising for energy harvesting and self-powering applications.

Conflicts of interest

The authors declare no conflicts of interest.

Acknowledgements

We gratefully acknowledge the support from the Royal Society Newton Advanced Fellowship (NA170184), the National Key Research and Development Program of China (2016YFA0203301) and the National Natural Science Foundation of China (21704095, 51625305).

References

1 H. Long, A. Harley-Trochimczyk, P. Thang, Z. Tang, T. Shi, A. Zettl, C. Carraro, M. A. Worsley and R. Maboudian, *Adv. Funct. Mater.*, 2016, **26**, 5158–5165.
2 W. Xia, C. Qu, Z. Liang, B. Zhao, S. Dai, B. Qiu, Y. Jiao, Q. Zhang, X. Huang, W. Guo, D. Dang, R. Zou, D. Xia, Q. Xu and M. Liu, *Nano Lett.*, 2017, **17**, 2788–2795.
3 C. Zhu, T. Y.-J. Han, E. B. Duoss, A. M. Golobic, J. D. Kuntz, C. M. Spadaccini and M. A. Worsley, *Nat. Commun.*, 2015, **6**, 6962.
4 X. Xu, H. Liang, F. Ming, Z. Qi, Y. Xie and Z. Wang, *ACS Catal.*, 2017, **7**, 6394–6399.
5 M. A. Worsley, S. J. Shin, M. D. Merrill, J. Lenhardt, A. J. Nelson, L. Y. Woo, A. E. Gash, T. F. Baumann and C. A. Orme, *ACS Nano*, 2015, **9**, 4698–4705.
6 X. Wu, J. Zhou, W. Xing, G. Wang, H. Cui, S. Zhuo, Q. Xue, Z. Yan and S. Z. Qiao, *J. Mater. Chem.*, 2012, **22**, 23186–23193.
7 G. Li, D. Dong, G. Hong, L. Yan, X. Zhang and W. Song, *Adv. Mater.*, 2019, **31**, 1901403.
8 G. Fu, X. Yan, Y. Chen, L. Xu, D. Sun, J.-M. Lee and Y. Tang, *Adv. Mater.*, 2018, **30**, 1704609.
9 G. He, M. Qiao, W. Li, Y. Lu, T. Zhao, R. Zou, B. Li, J. A. Darr, J. Hu, M.-M. Titirici and I. P. Parkin, *Adv. Sci.*, 2017, **4**, 1600214.
10 C. Hu, L. Song, Z. Zhang, N. Chen, Z. Feng and L. Qu, *Energy Environ. Sci.*, 2015, **8**, 31–54.
11 B. Wang, W. Al Abdulla, D. Wang and X. S. Zhao, *Energy Environ. Sci.*, 2015, **8**, 869–875.
12 T. Xu, Q. Han, Z. Cheng, J. Zhang and L. Qu, *Small Methods*, 2018, **2**, 1800108.
13 A. T. Liu, G. Zhang, A. L. Cottrill, Y. Kunai, A. Kaplan, P. Liu, V. B. Koman and M. S. Strano, *Adv. Energy Mater.*, 2018, **8**, 1802212.
14 F. F. Reuss, *Mem.Soc. Imp. Natur. Moscou*, 1809, **2**, 327–337.
15 F. Reuss, *Proc. Imperial Soc. Naturalists Mosc.*, 1809, **3**, 327–344.
16 S. Wall, *Curr. Opin. Colloid Interface Sci.*, 2010, **15**, 119–124.
17 G. A. H. Elton, *Proc. R. Soc. London, Ser. A*, 1949, **197**, 568–572.
18 S. Ghosh, A. K. Sood and N. Kumar, *Science*, 2003, **299**, 1042–1044.
19 (*a*) G. Xue, Y. Xu, T. Ding, J. Li, J. Yin, W. Fei, Y. Cao, J. Yu, L. Yuan, L. Gong, J. Chen, S. Deng, J. Zhou and W. Guo, *Nat. Nanotechnol.*, 2017, **12**, 317–321; (*b*) T. Ding, K. Liu, J. Li, G. Xue, Q. Chen, L. Huang, B. Hu and J. Zhou, *Adv. Funct. Mater.*, 2017, **27**, 1700551.
20 Z. Zhang, X. Li, J. Yin, Y. Xu, W. Fei, M. Xue, Q. Wang, J. Zhou and W. Guo, *Nat. Nanotechnol.*, 2018, **13**, 1109–1119.
21 J. Yin, X. Li, J. Yu, Z. Zhang, J. Zhou and W. Guo, *Nat. Nanotechnol.*, 2014, **9**, 378–383.
22 J. Pei, J. Huang, Z. Huang and K. Liu, *Sustainable Energy Fuels*, 2019, **3**, 599–610.

23 T. Xu, X. Ding, C. Shao, L. Song, T. Lin, X. Gao, J. Xue, Z. Zhang and L. Qu, *Small*, 2018, **14**, e1704473.
24 Y. Huang, H. Cheng, C. Yang, P. Zhang, Q. Liao, H. Yao, G. Shi and L. Qu, *Nat. Commun.*, 2018, **9**, 4166.
25 F. Zhao, Y. Liang, H. Cheng, L. Jiang and L. Qu, *Energy Environ. Sci.*, 2016, **9**, 912–916.
26 T. Xu, X. Ding, Y. Huang, C. Shao, L. Song, X. Gao, Z. Zhang and L. Qu, *Energy Environ. Sci.*, 2019, **12**, 972–978.
27 (*a*) Z. Liu, Z. Li, Z. Xu, Z. Xia, X. Hu, L. Kou, L. Peng, Y. Wei and C. Gao, *Chem. Mater.*, 2014, **26**, 6786–6795; (*b*) I. Andjelkovic, D. N. H. Tran, S. Kabiri, S. Azari, M. Markovic and D. Losic, *ACS Appl. Mater. Interfaces*, 2015, **7**, 9758–9766.
28 S. Yang, Y. Su, Y. Xu, Q. Wu, Y. Zhang, M. B. Raschke, M. Ren, Y. Chen, J. Wang, W. Guo, Y. Ron Shen and C. Tian, *J. Am. Chem. Soc.*, 2018, **140**, 13746–13752.
29 F. Meng, S. A. Morin and S. Jin, *J. Am. Chem. Soc.*, 2011, **133**, 8408–8411.
30 H.-P. Cong, X.-C. Ren, P. Wang and S.-H. Yu, *ACS Nano*, 2012, **6**, 2693–2703.
31 J. Yin, Z. Zhang, X. Li, J. Yu, J. Zhou, Y. Chen and W. Guo, *Nat. Commun.*, 2014, **5**, 3582.
32 F. Xiao, W. Li, L. Fang and D. Wang, *J. Hazard. Mater.*, 2016, **308**, 11–20.
33 M. C. Lu, J. N. Chen and C. P. Chang, *J. Hazard. Mater.*, 1999, **65**, 277–288.
34 T. R. Cook, D. K. Dogutan, S. Y. Reece, Y. Surendranath, T. S. Teets and D. G. Nocera, *Chem. Rev.*, 2010, **110**, 6474–6502.

